

Development of a Solar-Induced Fluorescence—Canopy Conductance Model and Its Application to Stomatal Reactive Nitrogen Deposition

Erin R. Delaria,[#] Bryan K. Place,[#] Alexander J. Turner, Qindan Zhu, Xiaomeng Jin, and Ronald C. Cohen*



Cite This: *ACS Earth Space Chem.* 2021, 5, 3414–3428



Read Online

ACCESS |



Metrics & More



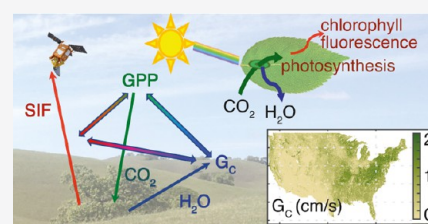
Article Recommendations



Supporting Information

ABSTRACT: The bidirectional exchange of gases between vegetation and the atmosphere is controlled by a variety of environmental factors and feedbacks that are entangled and difficult to quantify. As a result of this complexity, parameterizations of canopy conductance (G_c) in atmospheric models introduce large uncertainties and likely biases into representations of atmosphere–biosphere gas exchange. We present a novel representation of canopy conductance derived from measurements of solar-induced fluorescence (SIF) from the TROPOspheric Monitoring Instrument (TROPOMI). We show a strong linear correlation between GPP and G_c calculated using the Penman–Monteith theory, across a variety of ecosystem types in the AmeriFlux network. We couple this G_c –GPP correlation to previous research showing a strong linear correlation between SIF and GPP and estimate G_c at a 500 m spatial resolution across the continental United States. We also combine our model with surface estimates of NO_2 and PAN from WRF-Chem to estimate stomatal deposition fluxes of these gases. Our results suggest that satellite measurements of SIF can provide important constraints on model representations of stomatal activity and canopy gas exchange on regional and global scales.

KEYWORDS: canopy conductance, reactive nitrogen, deposition, solar-induced fluorescence, stomatal uptake, deposition



1. INTRODUCTION

The exchange of gases between the atmosphere and biosphere plays a fundamental role in determining the composition of the atmosphere. At the same time, changes in the atmospheric composition and climate provide important feedbacks that affect biological communities. This dynamic interaction between the atmosphere and biosphere is best exemplified by photosynthesis, which contributes one of the largest sinks of CO_2 for our atmosphere.¹ The simultaneous release of water vapor through transpiration also influences the water cycle and climate. Transpiration may return approximately 40% of incident precipitation back to the atmosphere, which in turn encourages later precipitation events.²

Transpiration takes place when water evaporates from the open stomata of leaves. This generally occurs in the presence of light to allow for the uptake of CO_2 during photosynthesis.^{3–5} Stomatal conductance thus plays a fundamental role in both the carbon and water cycles.^{6,7} During stomatal opening, other atmospheric gases, including ozone (O_3), reactive nitrogen (N_r), and volatile organic compounds, also diffuse in and out of plant leaves, affecting other chemical cycles.^{7–13} In particular, the canopy reduction of soil-emitted nitrogen has been shown to have a major influence on the nitrogen cycle.^{14–16}

Because the stomatal exchange of trace gases has a substantial impact on atmospheric composition, the accurate

representation of the stomatal conductance (g_s) in atmospheric models is essential.^{16,17} However, stomatal conductance is influenced by a variety of environmental factors (e.g., vapor pressure, soil water potential, light availability, CO_2 , O_3 , and season), making it difficult to include a fully mechanistic description in models.^{5,12,16,18–20} This is further complicated by diverse species-specific responses to these environmental factors. As a result, model representations of g_s are very complex and heavily parameterized, leading to a large degree of variability in representations of atmosphere–biosphere exchange of trace gases.^{19,21,22} As stomatal emission and uptake is a major term in the budgets of many trace gases, this lack of clarity limits our understanding of atmospheric composition.

The canopy conductance (G_c) can be thought of as the integrated sum of the stomatal conductance over all the leaves in the canopy. In the last 2 decades, remote sensing has become a valuable tool for estimating both G_c and evapotranspiration fluxes over large spatial scales.^{23–33} For example, Yebra et al. (2012) found that the normalized

Received: July 16, 2021

Revised: September 26, 2021

Accepted: October 26, 2021

Published: November 11, 2021



difference vegetation index, enhanced vegetation index, and normalized difference water index could explain 80% of the variance between the respective VI and G_c at 16 FLUXNET sites.³⁰ More recent studies have shown that retrievals of solar-induced fluorescence (SIF) from GOME-2 and TROPOMI can be used as a strong predictor of site-level and ecosystem-level G_c .^{26,32,33} Maes et al. (2020)³³ demonstrate that the G_c –SIF response may be universal across most ecosystem types.

Here, we present an empirical relationship between SIF retrievals from the TROPospheric Monitoring Instrument (TROPOMI) and G_c determined from the AmeriFlux network. The TROPOMI SIF retrievals we use are at a 500 m resolution—the highest resolution SIF data set available from satellite measurements. We show that a coupled SIF–GPP– G_c model can be used to estimate G_c across the continental United States (CONUS) during the 2018 growing season. A potential application of this model is to estimate the stomatal deposition of reactive nitrogen and the resulting impacts on the nitrogen cycle. Stomatal conductance has been shown to be the limiting factor in the deposition of NO₂ and peroxyacetyl nitrate (PAN). As such, the deposition of NO₂ and PAN scales linearly with stomatal conductance.^{7,8} Rates of deposition are rapid enough to affect the lifetimes of NO_x and PAN by more than 10%, making an accurate description of this pathway for removal essential to the understanding of tropospheric chemistry. With G_c inferred from remote sensing, the dry deposition flux of these important atmospheric trace gases can be constrained through measurements of their ambient concentrations and the canopy conductance (G_c). To assess spatial and temporal patterns in the dry deposition of NO_x and PAN, we couple our SIF–GPP– G_c model with a chemical transport model (CTM) to estimate the dry deposition of NO₂ and PAN over the continental United States.

2. METHODS

2.1. CO₂ flux Data. Half-hourly surface energy flux, meteorological, and CO₂ fluxes and products were collected from the AmeriFlux website (<https://AmeriFlux.lbl.gov/data/download-data/>). A total of 154 sites across the CONUS contained measurements of the variables needed to carry out the study (see Section 2.2). The final flux data set encompassed the following land cover classes—deciduous broadleaf forests (18 sites), evergreen needleleaf forests (34 sites), mixed forests (7 sites), croplands (27 sites), grasslands (30 sites), open and closed shrublands (21 sites), and wetlands (17 sites). Figure 1 shows the geographic distribution and land type of all the sites used.

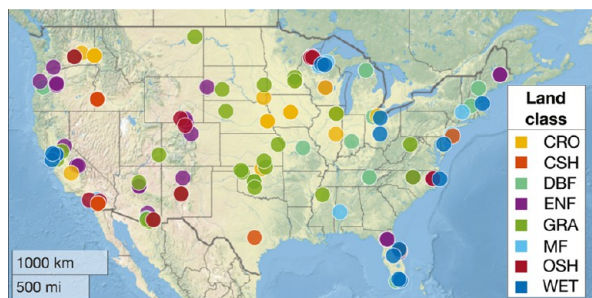


Figure 1. Location and IGBP land class of all the AmeriFlux sites across CONUS used to carry out the study.

2.2. Calculations of Canopy Conductance (G_c) and Gross Primary Productivity (GPP). Canopy conductance (G_c) was calculated at each site at the time of TROPOMI overpass (LT 13:30) using the inverted Penman–Monteith equation (eq 1), which uses a surface energy flux and mass balance approach to estimate the surface conductance.³⁴ The Penman–Monteith equation estimates G_c using measurements or calculations of the net radiation flux (R_n), the soil heat flux (G), the latent energy flux (LE), air density (ρ_a), specific heat capacity of air (C_p), vapor pressure deficit (VPD) (δ_e), conductivity of air (g_a), the slope of the saturated vapor pressure curve (Δ), and the psychrometric constant (γ).

$$\frac{1}{G_c} = \frac{\Delta(R_n - G) + \rho_a C_p \delta_e g_a - \Delta LE - \gamma LE}{\gamma g_a LE} \quad (1)$$

Measurements of R_n , G , and LE were provided directly from each of the sites. In instances where one of the three fluxes was not reported, the sensible heat flux (H) was used to calculate the missing flux through the surface flux balance relationship (eq 2). Measurements of temperature (T), pressure (P), and relative humidity (RH) were used to calculate ρ_a , γ , δ_e , and Δ via 3.

$$R_n - G - H - LE = 0 \quad (2)$$

$$\rho_a = \frac{1000P}{287.058(T + 273.15)} \quad (3)$$

$$\gamma = 0.66P \quad (4)$$

$$\delta_e = (1 - \text{RH})0.61121 e^{(18.678 - \frac{T}{234.5})(\frac{T}{257.14 + T})} \quad (5)$$

$$\Delta = \frac{\partial \delta_e}{\partial T} \quad (6)$$

Measurement height (z), displacement height (d), roughness length to momentum transfer (z_{om}), roughness length to heat transfer (z_{oh}), von Karman's constant (k), and wind speed (U) were used to determine g_a through eq 7. The values of d , z_{om} , and z_{oh} were estimated as $0.66h$, $0.123h$, and $0.0123h$, respectively, where h represents the canopy height. Stability corrections using measurements of air and surface temperature were also performed on eq 7 following recommended factors by Monteith (1973) and Hatfield et al. (1983).^{35,36} The stability-corrected G_c values differed from the original G_c values on average by less than 2% (Figure S1). Because the method showed low sensitivity to the calculation of g_a and only half of the total AmeriFlux sites used in the analysis report surface temperature measurements, the calculation of G_c was carried forward without the use of stability-corrected g_a values.

$$\frac{1}{g_a} = \frac{\ln \frac{z-d}{z_{om}} \ln \frac{z-d}{z_{oh}}}{k^2 U} \quad (7)$$

The Penman–Monteith derivation of G_c encompasses both transpiration and evaporation processes. We applied a precipitation filter to remove days where surface evaporation may have contributed measurably toward the total surface conductance. The filter removed any 7-day period when the amount of precipitation exceeded the 90th percentile of the data set on the first day of the screened period. An interquartile range outlier test was then applied to the screened G_c data set.

It should be noted that recent studies have suggested that the inverted Penman–Monteith derivation of G_c introduces uncertainties due to energy imbalance (i.e., $R_n - G - H - LE \neq 0$).^{37–39} However, Penman–Monteith is still the most commonly used method for deriving G_c from surface energy and water vapor fluxes.^{26,32,33,40} The effect of energy imbalance is also likely to be minimal in our work, as the energy imbalance is lesser in the afternoon (during the time of TROPOMI overpass).³⁹

Gross primary production (GPP) measurements were obtained directly from each site or calculated using measurements of net ecosystem exchange (NEE) and ecosystem respiration (RECO). At sites that did not partition NEE to GPP and RECO, we estimated GPP by equating average nighttime CO_2 fluxes to RECO and subtracting this from daytime CO_2 fluxes: $\text{GPP} = \text{NEE} - \text{NEE}_{\text{night}}$.⁴¹

To correspond with TROPOMI's early afternoon overpass time, G_c and GPP were aggregated into daily midday estimates by taking the median values between 12:30 and 14:30 local time each day. Final smoothed data sets were produced by calculating a 14-day moving average of G_c and GPP.

2.3. Observations of Solar-Induced Chlorophyll Fluorescence from TROPOMI. We use observations of SIF from the TROPOMI instrument on the Sentinel-5P satellite.⁴² Briefly, TROPOMI is a nadir-viewing imaging spectrometer in a 16-day sun-synchronous orbit with bands in the UV, visible, and near-infrared. The TROPOMI ground swath is 2600 km across track and the nadir footprint size is 5.6 km along-track and 3.5 km across track. SIF retrievals are made over a small window in the far red at 740 nm. Köhler et al.⁴³ developed the first retrievals of SIF from TROPOMI. We use the 500 m downsampled SIF data described by Turner et al.^{44,45} Turner et al.^{44,45} used data from multiple viewing geometries to obtain higher resolution than the native TROPOMI footprint size and then further downsampled the SIF using a sub-grid weighting based on high-resolution observations of vegetation from the moderate resolution imaging spectroradiometer (MODIS). The end result is a 500 m daily estimate of SIF that represents a 16-day moving average. Turner et al.^{44,45} also observed a linear relationship between early afternoon GPP data from AmeriFlux sites and coincident observations of SIF from TROPOMI.

2.4. CTM Simulations. The Weather Research and Forecast Model coupled with chemistry (WRF-Chem) version 3.5.1 was used to simulate hourly surface NO_2 and PAN concentrations and meteorology. Simulations encompassed the CONUS domain with a horizontal resolution of 12×12 km and 29 vertical layers. The simulation period was from February 2018 to February 2019. A customized version of the Regional Atmospheric Chemistry Mechanism version 2 (RACM2) was employed to model the chemistry, and the details are described in Zare et al. (2018).⁴⁶ The North American Regional Reanalysis (NARR) provides initial meteorological and boundary conditions and was nudged every 3 h to constrain the meteorological fields. The chemical initial and boundary conditions were constrained by The Community Atmosphere Model with Chemistry (CAM-chem^{47,48}). The Model of Emissions of Gases and Aerosols from Nature (MEGAN) was used to determine the biogenic emissions, and the National Emissions Inventory 2011 (NEI 11) was used to describe anthropogenic emissions. To account for the annual emission reduction, an additional scaling factor was applied to scale the total emission to the reported emission

at model year from the United States Environmental Protection Agency.⁴⁹

We also use the GEOS-Chem CTM (v12.7.0) to compare fluxes and deposition velocities of NO_2 and PAN. The GEOS-Chem model used is driven by the assimilated meteorological fields from the Goddard Earth Observation System Forward Processing products (GEOS-FP) at $0.25^\circ \times 0.3125^\circ$ spatial resolution. We conduct nested GEOS-Chem simulations over North America (10°N – 70°N , 140°W – 40°W) for summer 2018. The boundary conditions are generated from a global simulation at $2^\circ \times 2.5^\circ$ resolution with a 1-year spin-up. We use the standard tropospheric chemical scheme that includes detailed NO_x –hydrocarbon–aerosol chemistry, as described in Travis et al. (2016)⁵⁰ and Fisher et al. (2016).⁵¹ The NEI2011 inventory is used for U.S. anthropogenic emissions and scaled to 2018 level based on the national emission trends (EPA, 2018).

3. DEVELOPMENT OF A COUPLED G_c –GPP–SIF MODEL

Previous works by Shan et al. (2019) and Maes et al. (2020) have shown that SIF retrievals from the GOME-2 instruments onboard the EUMETSAT's MetOp series satellites are strongly correlated with G_c .^{26,33} Retrievals from TROPOMI (Sentinel-5P satellite) were also used more recently to probe the G_c –SIF relationship.³² The authors of this study found a strong correlation between these variables across three different field sites.³² The goal of the current work is to build on these bodies of work and determine an empirical relationship between SIF retrievals from TROPOMI and G_c across a wide range of ecosystem types and locations. Initially, we explored a direct SIF– G_c relationship. However, limited measurements of the parameters necessary for the calculation of G_c across the AmeriFlux network that coincided with TROPOMI's measurement period (2018–2020) made it difficult to accurately describe the relationship. In order to provide better spatial coverage and to better capture the SIF– G_c response in a variety of ecosystems, we correlated G_c and SIF (a proxy for GPP) indirectly through GPP with multiyear measurements across the AmeriFlux network. The validity of this approach is demonstrated in Figure S2, which shows direct correlations of SIF and G_c , SIF and GPP, and GPP and G_c using the limited measurements from AmeriFlux sites that coincided with TROPOMI's active period.

The theory and methods behind the TROPOMI SIF–GPP relationship used in this work are provided in Turner et al. (2021).⁴⁵ The focus of the current work is to establish a quantitative relationship between SIF and G_c from the linear correlations between SIF and GPP and GPP and G_c . The linear correlation between GPP and SIF has been discussed in a number of recent publications.^{44,45,52,53} There has, however, been some evidence that there is divergence between GPP and SIF at the leaf-level under low light intensities and certain environmental conditions.^{54,55} Recently, Magney et al. (2020) highlighted that a linear relationship between GPP and SIF is expected at high light levels under conditions of both stressed and nonstressed leaves and sunlit and shaded leaves. These high light levels are characteristic of the early afternoon during the time of TROPOMI overpass and SIF observations. This potentially explains why SIF and GPP are strongly correlated when using space-borne measurements, yet decouple at sub-diurnal scales using surface measurements.

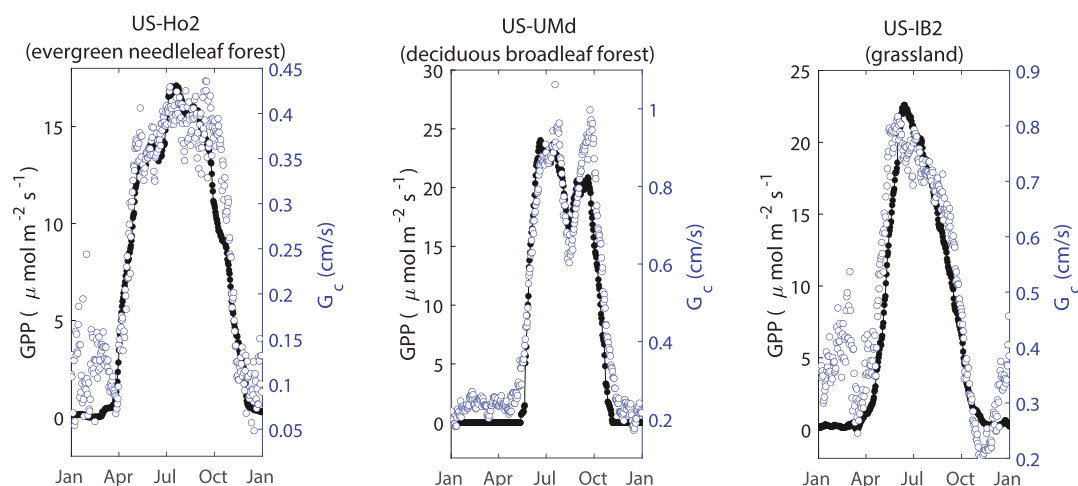


Figure 2. Gross primary productivity (GPP, black closed circles) and canopy conductance (G_c , open blue circles) averaged by day of year over the data record for three representative AmeriFlux sites.

3.1. Covariation of GPP and G_c at AmeriFlux Sites.

Leaf-level studies have shown that stomatal conductance to water vapor and CO_2 assimilation are strongly correlated.^{57–60} This empirical relationship is typically described through the Ball–Berry (BB) model (eq 8), where g_s is the stomatal conductance to water vapor, A^* is the CO_2 assimilation rate or leaf photosynthesis rate adjusted for environmental variables, m is the Ball–Berry parameter and slope of best fit, and g_0 is the minimum stomatal conductance intercept.⁵⁷

$$g_s = mA^* + g_0 \quad (8)$$

Field measurements have shown that the Ball–Berry model may be extended to the canopy-level and can be used as a good predictor of canopy conductance and canopy CO_2 assimilation.^{61–65} Under the big leaf model framework (i.e., treating a canopy as one big leaf), g_s and A^* may be replaced by G_c and GPP, respectively, in eq 8, assuming there is little contribution from canopy morphology and that the slope of the response is insensitive to changes in environmental variables.^{26,66} Following these assumptions, one would anticipate a linear relationship between GPP and G_c .

Figure 2 shows a multiyear average time series of GPP and G_c for select evergreen needleleaf, deciduous broadleaf, and grassland AmeriFlux sites. This figure demonstrates that GPP and G_c correlate well ($R = 0.68–0.81$) with one another during the growing season (April–October) at the three sites. Subtle changes in CO_2 assimilation over the growing season, such as the average increase in GPP seen in June at US-Ho2 and the decrease in GPP during August at US-UMd, are captured in the G_c model. A higher degree of variability around zero GPP was observed during the winter months (November–March) at these sites and also across the entire AmeriFlux network. The highly variable wintertime G_c calculations are likely artifacts and represent surface evaporation fluxes instead of transpiration fluxes during this time period. This hypothesis is supported by measurements of low leaf area indices across the AmeriFlux network during winter months (Figure S3). Subsequently, all site flux data were screened using a solar zenith angle of 35° to eliminate contributions from the winter months in order to more accurately assess the GPP– G_c relationship during the growing season.

In general, we observe moderate-high linear correlations between GPP and G_c at individual AmeriFlux sites during the

growing season (Figure 3). The average correlation coefficient (R) across all sites was determined to be 0.7 ± 0.2 . The

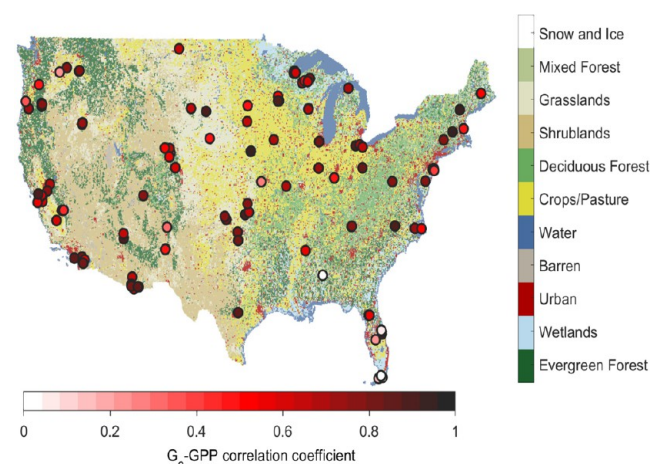


Figure 3. Landcover types over the continental United States from the National Land Cover Database (NLCD) and AmeriFlux site locations (circles). AmeriFlux sites are colored by the correlation coefficient for the canopy conductance (G_c)–gross primary productivity (GPP) relationship.

strongest site-level GPP– G_c relationships and the lowest average variance was observed in cropland ecosystems ($R = 0.74 \pm 0.09$). The weakest correlations and the highest average variance was observed at the wetland sites (average correlation = 0.5 ± 0.3). The higher average correlations observed at the cropland sites may be a consequence of the Penman–Monteith G_c model being optimized for agricultural systems. The weaker GPP– G_c correlations determined at the wetland sites were likely driven by the contribution of evaporation fluxes to the estimated G_c fluxes.

The correlations we report are of the same magnitude as other studies ($R = 0.68–0.94$) that investigated correlations between canopy-scale g_s and A^* .^{62,64,65} Observed correlations in the previous studies were typically higher because A^* values were adjusted using measurements of ambient $[\text{CO}_2]$ and $[\text{H}_2\text{O}]$ prior to the correlations in order to better represent the g_s – A^* relationship through the Ball–Berry model. It has also been recommended to adjust A^* by relative humidity, a CO_2

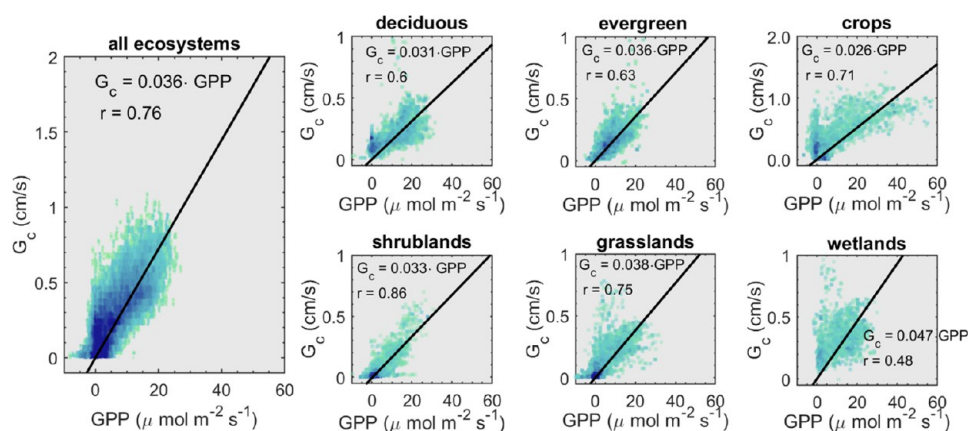


Figure 4. Canopy conductance–gross primary productivity (GPP) relationship for six ecosystem types and all sites combined as identified by the International Geosphere–Biosphere Programme (IGBP) classification. Open and closed shrublands are combined to one shrubland land type. IGBP classes (e.g., evergreen broadleaf, mixed forest, and woody savanna) were excluded if fewer than six sites of the class had available data. These sites were included in the plot for all ecosystems. Data are colored by density. Black lines show the linear G_c –GPP relationship fitted with a bisquare regression. Slopes and correlation coefficients are identified on each plot.

compensation point, VPD, and a stomatal optimization constant to better capture the g_s – A^* relationship.^{21,57–60} Adjustment of our model with measurements of VPD did lead to improvements in the correlation between GPP and G_c at most sites. However, for the purpose of our investigation we opted to not adjust the reported GPP– G_c model with VPD and other environmental variables to avoid further complexity in the model. Our unadjusted GPP– G_c model demonstrated reasonable efficacy across sites as GPP generally explained over 60% of the variability in G_c .

3.2. Ecosystem-Level Relationships between G_c and GPP. The strong linear correlations that we determined between the multiyear GPP and G_c data sets at the 154 AmeriFlux sites (Figure 3) suggest that the GPP– G_c relationship can be sufficiently described using a linear relationship at the site-level. To test whether unique GPP– G_c relationships existed at the ecosystem-level, the sites were grouped by ecosystem type for further analysis. Mixed forest sites were not carried forward in the ecosystem-level analysis due to the limited number of mixed forest sites in the data set ($N = 7$) and the likelihood that the GPP– G_c relationship was captured in the analysis of other forested sites. Figure 4 shows the slopes of the lines of best fit forced through a zero intercept for the GPP– G_c relationship across all sites for each ecosystem type. The slopes determined from these lines of best fit ranged from 0.026 to 0.047 [($\text{cm s}^{-1} \text{H}_2\text{O}$) ($\mu\text{mol}^{-1} \text{CO}_2 \text{m}^2 \text{s}$)] and correlations ranged from 0.48 to 0.86 between ecosystems. Wetland ecosystems had the highest slope and poorest correlation, which was likely driven by the influence of surface water evaporation. The GPP– G_c response was the smallest in the cropland ecosystems and the cropland sites seemed to exhibit a lower correlation at the ecosystem-level than at the site-level. The lower slope observed in the crop GPP– G_c relationship seems to be driven by sites that showed very high CO_2 assimilation. High levels of GPP could be indicative of an environment with elevated CO_2 levels, which have shown to cause deviations from linearity in the Ball–Berry relationship.⁶⁷ A histogram showing the distribution of all GPP/ G_c ratios that we calculated using our method can be found in Figure S4. We did not identify any statistical evidence that the GPP– G_c relationship was distinct for different ecosystems. Figure 4 shows the line of best fit through all the GPP and G_c

flux data. An overall slope of 0.036 [($\text{cm s}^{-1} \text{H}_2\text{O}$) ($\mu\text{mol}^{-1} \text{CO}_2 \text{m}^2 \text{s}$)] and a linear correlation of 0.76 was determined from the line of best fit through all ecosystem-level data.

Although the Ball–Berry model (eq 8) suggests a minimum conductance intercept (g_0), we conducted the ecosystem-level analysis under the assumption $g_0 = 0$. In practice, this was enforced through a linear regression with no intercept term. This assumption was justified by examining site-level fits of the G_c –GPP relationship using data from all months of the year. The solar zenith angle filter was not applied for this analysis, as some sites did not have sufficient variation in GPP after applying the filter to calculate a statistically significant intercept. The median intercepts (g_0) from all sites of a certain ecosystem type were substantially larger than the nighttime canopy conductance, when PAR and GPP are both zero (see Table S1). We attribute a larger fitted intercept than the nighttime canopy conductance to a larger contribution from surface evaporation, rather than transpiration, during the wintertime. As such, the intercepts identified by the model are likely a representative of stomatal and nonstomatal factors. This is particularly evident at sites such as US-UMd (Figure 2), where there is a nonzero winter canopy conductance, despite this being a deciduous forest that would have a very low LAI during the winter. Furthermore, the Ball–Berry parameters g_0 and m have been found to have a seasonal dependence in some species.^{6,67} The g_s – A^* relationship has also been shown to be nonlinear at very low light intensities, resulting in differences between g_0 derived via linear regression and g_0 measured during the nighttime.⁶⁸ The SIF–GPP relationship is also known to have nonlinearities at low light intensities.⁵⁶ Our goal is to offer constraints on stomatal activity using satellite SIF measurements, which is likely to be more significant and more accurate at higher light levels and LAI, and we therefore prioritize prediction of G_c during the growing season. To support this claim, we carried forward an ecosystem-wide intercept from the line of best fit in the calculation of NO_2 deposition fluxes (see Section 5.2 for additional details) for the months of January and June 2018 (Figures S6 and S7). These figures support the idea that NO_2 flux estimates would be elevated in areas of low leaf cover ($\text{LAI} < 2 \text{ m}^{-2} \text{ m}^2$), particularly in the wintertime, with the inclusion of an intercept. The estimated fluxes also exhibit little variation in

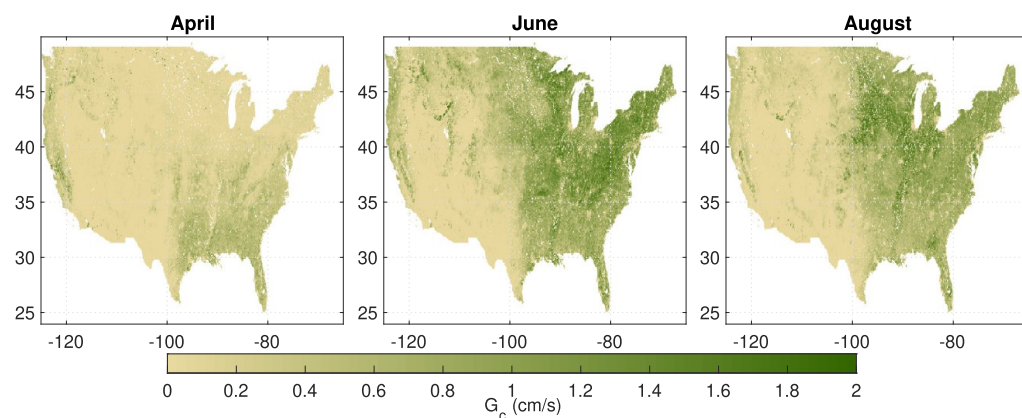


Figure 5. Monthly averaged canopy conductances (G_c) derived from TROPOMI SIF measurements for the months of April (left), June (middle), and August (right) of 2018. G_c averages are at the time of TROPOMI overpass (13:30 LT).

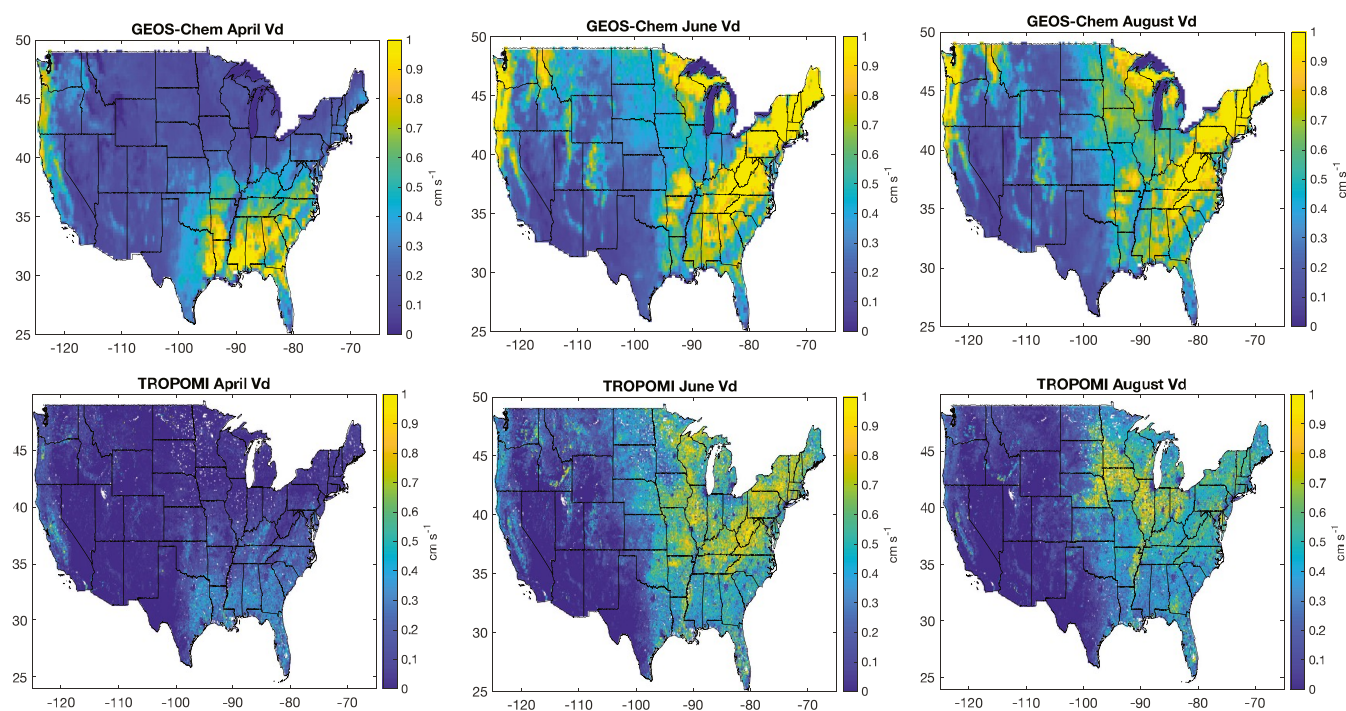


Figure 6. Average 2018 monthly NO_2 deposition velocities (V_d) as predicted by (top) GEOS-Chem and (bottom) TROPOMI SIF measurements at the time of TROPOMI's overpass (LT 13:30). It should be noted that GEOS-Chem deposition velocities include surface nonstomatal deposition.

fluxes (<10%) in areas of high leaf area ($\text{LAI} > 2 \text{ m}^{-2} \text{ m}^2$) during the summertime when an intercept is considered in the model.

In a recent review of leaf-level studies exploring the g_s – A^* relationship, Miner et al. (2017)⁶⁷ also describe that the Ball–Berry parameter (m) can vary under differing environmental conditions (e.g., drought-stress, elevated CO_2 levels) and that the Ball–Berry parameter has also been shown to differ across plant species. However, the ecosystem-level fits we present in Figure 4 show that on average, the GPP – G_c relationship converges to a single slope across all ecosystems. Based on these findings we carried a scaling factor of 0.036 forward to describe the GPP – G_c relationship for all ecosystems.

4. MODELING G_c WITH TROPOMI SIF

Combining our observations that show G_c scales linearly with GPP with previous research that shows SIF scales linearly with

GPP , we propose: $G_c \propto \text{SIF}$. The final G_c –SIF relationship we determine is shown in eq 9, where β is an ecosystem-specific scaling factor to convert SIF into GPP . β is derived from the SIF– GPP relationship inferred from comparison with AmeriFlux GPP , multiplied by the fraction of the grid cell represented by the ecosystem type. The reader is directed to Turner et al. (2021) for a more complete description of β .⁴⁵

$$G_c = 0.036 \times \beta \times \text{SIF} \quad (9)$$

Equation 9 gives an estimate of G_c during TROPOMI's overpass time (approximately 13:30 local time). Monthly averaged 13:30 LT G_c values for the months of April, June, and August 2018 across CONUS are presented in Figure 5 and the annual 2018 average can be found in the Supporting Information (Figure S5). The SIF– G_c model captures both the onset and decline of the growing season as the months progress from April to August. Biological activity (i.e., G_c and

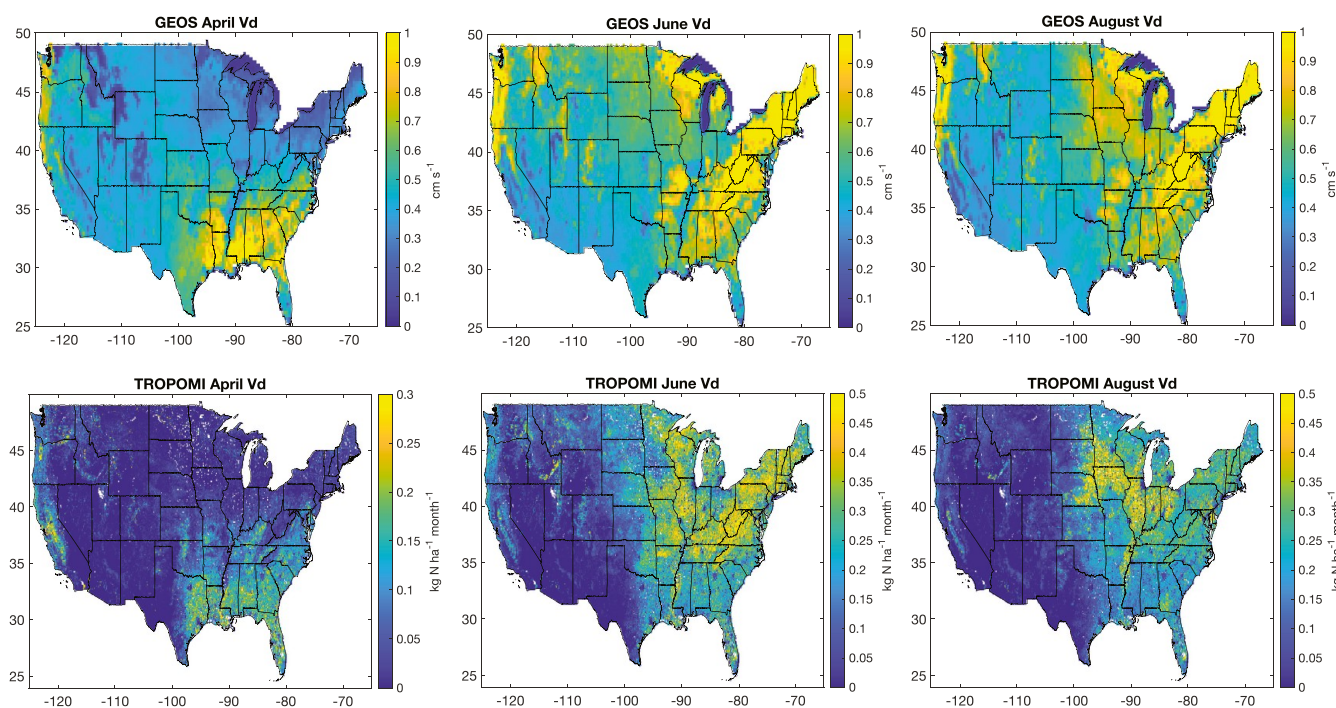


Figure 7. Average 2018 monthly PAN deposition velocities (V_d) as predicted by (top) GEOS-Chem and (bottom) TROPOMI SIF measurements at the time of TROPOMI's overpass (LT 13:30). It should be noted that GEOS-Chem deposition velocities include surface nonstomatal deposition.

GPP) was seen to be much higher in the east than the west. This general observation is consistent with other studies that have estimated G_c and GPP across CONUS.^{30,45,69} Fine features such as the California Central Valley agricultural region and the Corn Belt in the Midwest can also be seen in Figure 5. A G_c range of 0–2 cm s^{-1} was determined by the SIF– G_c model across CONUS. These G_c predictions fell well within the range of observations across the AmeriFlux network.

To demonstrate the model's robustness, we tested how the G_c model would respond to the use of a single scaling factor for all ecosystems versus ecosystem-specific scaling factors, and to an exponential versus linear model fit. An exponential fit was chosen for the sensitivity analysis to reflect the nonlinearities that have been reported at high and low levels of GPP in the G_c –GPP relationship.^{67,68} For the first sensitivity analysis, we show the difference between 2018 averaged G_c across CONUS using a factor of 0.036 versus ecosystem-specific slopes determined from Figure 4 in Figure S8. We observe approximately a 10% decrease in G_c and NO_2 fluxes (see Section 5.2) in crop regions and an increase of approximately 20% in wetlands regions (Figure S8). The slopes for mixed forests, deciduous broadleaf forests, evergreen needleleaf forests, grasslands, and shrublands differ by less than 10%. For the second sensitivity test, we show the difference between 2018 averaged G_c and calculated NO_2 fluxes when using an exponential fit in the place of a linear fit in Figure S9. Percentage changes in G_c of up to 20% were observed in some regions; however, in regions of high leaf cover, G_c was seen to vary by 10% or less. The percent changes in annual NO_2 -estimated fluxes were also typically less than 10%. All of these variances from the linear model are small compared to the difference between our proposed model and the predominant models describing N fluxes (Figures 6, 7, and S10).

Stomatal activity is typically modeled as a function of light intensity and temperature using the formulation of Wesely

(1989) in many atmospheric CTMs (e.g., WRF-Chem and GEOS-Chem). Additional considerations of VPD and soil water availability have been demonstrated to substantially improve the estimates of ozone, carbon, and water atmosphere–biosphere exchange.^{12,17,71,72} However, these parameterizations fail to adequately represent the impact of drought on stomatal behavior. Approaches have also been described that represent stomatal conductance and transpiration by considering water use efficiency and water transport along the soil, plant, and atmosphere continuum.^{22,72} These considerations have provided improved representations of stomatal behavior from a physiological and mechanistic perspective but are typically heavily parameterized and require inputs of many plant, soil, and meteorological measurements. Another common approach to modeling stomatal conductance is through the coupling of the Farquhar photosynthesis model with the Ball–Berry model.⁵⁷ This approach requires knowledge of the maximum carboxylation rate and maximum electron-transfer rate, which are also difficult to determine at the ecosystem level.

To overcome limitations in stomatal conductance models, some investigations have explored the use of space-borne measurements to represent G_c . Yebra et al. (2012) found that vegetation indices (VIs) derived from MODIS could be used to compute global canopy conductance.³⁰ The results we obtain for G_c over CONUS are very similar in magnitude and spatial distribution as the midday averages reported by Yebra et al. between 2001 and 2011. In our study, as well as in that of Yebra et al., maximum G_c occurs in the eastern United States, where yearly average midday G_c is 0.6–0.7 cm/s (Figure S5). We, however, report lower yearly average G_c (~ 0.4 cm/s) compared to ~ 0.8 cm/s in the Pacific Northwest. This difference may in part be the result of a decline in the forest productivity in western forests over the past decade.^{73,74} We also consider it likely that the use of VIs by Yebra et al. may

have resulted in an overestimation of yearly average G_c for the evergreen forests of the Pacific Northwest. The largest deviation in SIF and V_i occurs for evergreen forests, with V_i showing little seasonal variation for winter-dormant evergreen forests.⁵²

SIF has been shown to be a robust predictor of ecosystem transpiration.^{33,40,75} Maes et al. (2020)³³ demonstrated that SIF and transpiration are highly correlated, with SIF predicting transpiration more reliably than any other satellite product. This relationship is determined by temperature and water use efficiency.³³ The value of SIF in directly determining G_c has also been previously demonstrated.^{26,32,40} Shan et al. (2019) show that SIF and G_c co-vary and that the strength of the relationship improves when the data are aggregated on longer timescales (>1 day). The authors propose that although their model is unable to provide information about dynamic changes in G_c , it reliably represents seasonal behavior. Similarly, our SIF– G_c model may not capture the dynamic response of G_c to environmental variables on daily and shorter timescales but can reasonably represent weekly, monthly, seasonal, and yearly changes. Another limitation noted by Shan et al. (2019) is that their SIF– G_c model may not accurately capture changes in the Ball–Berry parameter (m). Our approach to aggregating data somewhat overcomes this limitation by deriving m using a large-scale multiyear data set, as opposed to prescribing a value for m based on previous ecosystem measurements. Shan et al. (2021) extended the findings of Shan et al. (2019) and developed an empirical model linking G_c , SIF, and VPD at a deciduous broadleaf site and two wheat cropland locations. They show that the correlation between SIF and $G_c \times \text{VPD}^{0.5}$ is stronger than the link between G_c and SIF alone. Damm et al.⁴⁰ also found a strong relationship between SIF and transpiration and suggest that this relationship covaries with biotic and abiotic drivers, especially R_n and LAI. We, however, chose to not include VPD, R_n , or LAI, in our model, as this would also require accurate retrievals of temperature, relative humidity, and R_n over large spatial scales. Furthermore, Shan et al. (2021) also show that the difference between the SIF– G_c and SIF– $G_c \times \text{VPD}^{0.5}$ correlations is minimal during the early afternoon, when SIF– G_c correlations are maximal. Although our approach does not represent nonlinearities in the SIF– G_c relationship or changes in m with environmental conditions, it more adequately predicts average regional behavior with minimal parameters, making our approach especially applicable to large spatial and temporal scales.

The ability of SIF to represent G_c eliminates the need for modeling stomatal behavior with parameters for land type and meteorology, making SIF a powerful tool for predicting canopy conductance across large spatial regions. This has particular potential applications to the atmospheric lifetime and composition of depositing species, such as ozone, NO_2 , and peroxy nitrates. We propose that that consideration of SIF-derived G_c can offer improved constraints on stomatal deposition in global and regional CTMs. Further improvements of SIF-derived G_c across large spatial regions could be achieved with advancements in retrievals of additional environmental drivers.^{33,40,75}

5. APPLICATION OF TROPOMI SIF-DERIVED G_c TO STOMATAL N DEPOSITION OVER CONUS

While the wet deposition of reactive nitrogen (N_r) is monitored across North America through the US National Atmospheric Deposition Program (NADP) and the Canadian

Air and Precipitation Monitoring Network (CAPMoN),^{76,77} measurements of the air–surface exchange of N_r with vegetation remain scarce.^{78–81} Wet deposition and throughfall measurements have provided estimates of the wet and dry deposition of N_r to vegetation surfaces.^{82,83} These measurements can be used to quantify the surface deposition of nitrogen oxide gases, such as HNO_3 , but cannot capture the deposition of N_r through leaf stomata.

The current understanding of reactive nitrogen deposition to leaf stomata at a canopy and regional scale is based on an outdated resistance model approach that is poorly constrained and heavily parameterized.⁷⁰ In the following sections, we demonstrate the potential application of our G_c –SIF model as a tool for improving quantitative assessments of the magnitude, spatial, and temporal patterns of the stomatal deposition of N_r . We first discuss the derivation of stomatal NO_2 and PAN fluxes across CONUS. We then offer an analysis of how the stomatal deposition of NO_2 and PAN affects the atmospheric lifetime of these N_r species.

5.1. NO_2 and PAN Deposition Velocities. Controlled laboratory NO_2 and PAN deposition experiments to vegetation have found that the deposition of these N_r compounds mainly proceeds through stomatal uptake and that deposition scales directly with stomatal conductance.^{7,8,84–86} Surface deposition of these compounds has also been observed but is suggested to be a minor deposition pathway. For example, Delaria et al. (2020) and Place et al. (2020) investigated NO_2 and PAN deposition to 14 tree species grown under a variety of conditions and report a consistent relationship between the deposition velocities (V_d) of these gases and stomatal conductance (g_s). NO_2 and PAN were found to have deposition velocities equal to $0.56g_s$ and $0.3g_s$, respectively, with uncertainties in the relationships of less than 10%. It is possible that non woody herbaceous plants (e.g., crops and grasses) and C4 plants may process reactive nitrogen in a different manner than the tree species examined by Delaria et al., 2020 and Place et al., 2020. We are not aware of a mechanistic reason to expect that this would be the case, but further studies are needed to understand the scale factors appropriate for crops and to confirm that stomatal uptake is the only important mechanism for crops and grasses. Using the relationships determined from these studies, we estimate the canopy-level V_d 's for NO_2 and PAN as $0.56G_c$ and $0.3G_c$, respectively, from the SIF-derived G_c measurements across CONUS. We provide a comparison of these predicted V_d values to those predicted by GEOS-Chem at a local time of 13:30 in Figures 6 and 7. Deposition in GEOS-Chem is described through the Wesely resistance model, which models deposition through an aerodynamic resistance term, boundary layer resistance term, and a surface deposition resistance term. At an LT of 13:30, atmospheric conditions are expected to be largely unstable and the deposition rates of NO_2 and PAN are likely limited by surface deposition. Surface deposition in GEOS-Chem is heavily parameterized and encompasses both stomatal and nonstomatal pathways, and as such cannot offer a direct comparison with SIF-derived G_c but can be used to infer differences between the two approaches.

In general, there is good agreement between the spatial distribution of V_d implied by GEOS-Chem and TROPOMI SIF for both PAN and NO_2 (Figures 6 and 7). The deposition rates for NO_2 and PAN predicted by GEOS-Chem, however, tend to be much higher (up to a factor of 2 for PAN) than those predicted by TROPOMI in most locations. The higher

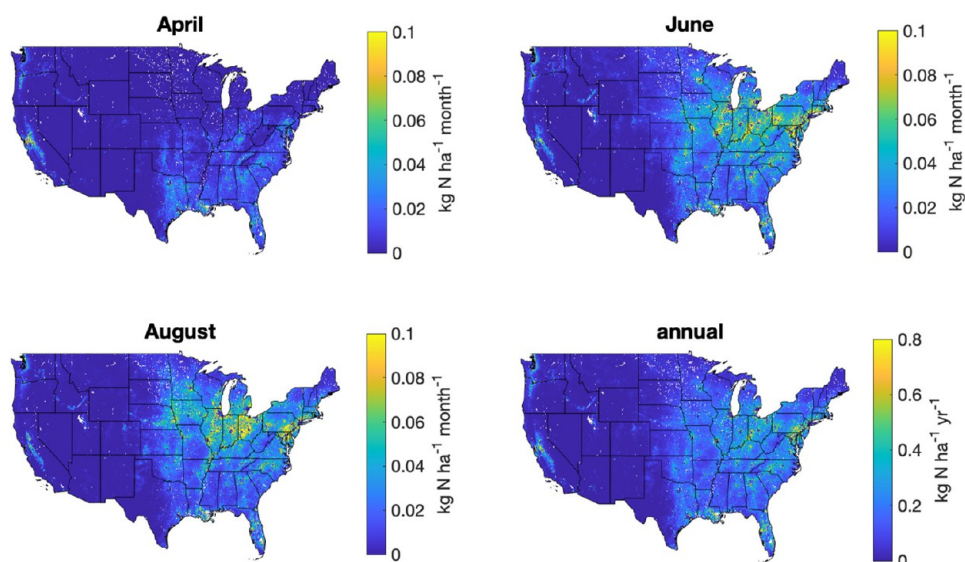


Figure 8. Estimated NO_2 stomatal fluxes over CONUS for the months of (a) April, (b) June, and (c) August as well as the (d) annual estimated NO_2 stomatal fluxes for 2018. Estimates were derived using TROPOMI SIF measurements and WRF-Chem NO_2 surface concentrations and meteorological outputs, as described in Section 5.1.

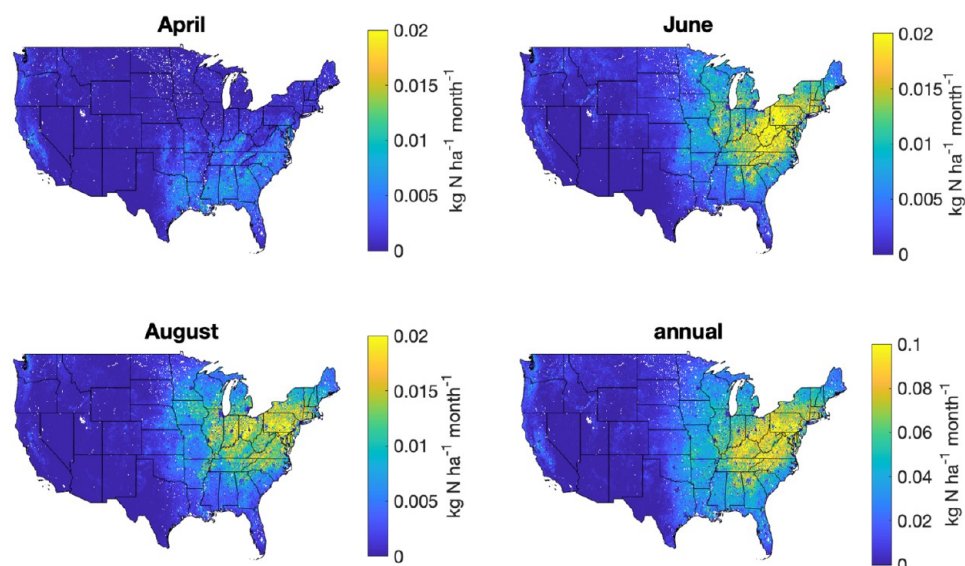


Figure 9. Estimated PAN stomatal fluxes over CONUS for the months of (a) April, (b) June, and (c) August as well as the (d) annual estimated NO_2 stomatal fluxes for 2018. Estimates were derived using TROPOMI SIF measurements and WRF-Chem PAN surface concentrations and meteorological outputs, as described in Section 5.2.

estimates in V_d rates by GEOS-Chem are likely due to the inclusion of considerable cuticular and surface deposition (e.g., to soil, branch/cuticle surfaces) terms used in GEOS-Chem. Figure 6 also shows that GEOS-Chem seems to disproportionately overestimate NO_2 deposition in the western United States during the late summer compared to mid-summer. This effect could be driven by the way the Wesely model parameterizes stomatal deposition, which neglects the effects from drought stress on stomatal uptake caused by low soil and air moisture. Stomatal conductance models that are more heavily parameterized have been shown to reproduce stomatal rates more accurately.¹⁶ One key advantage of the SIF- G_c fitting model is that it is able to capture real-time changes in G_c induced by the changing environmental and biological variables. We also see in Figure 6 that GEOS-Chem may be underestimating NO_2 deposition in the Corn Belt of the

Midwest and the California Central Valley and is likely not capturing the full extent of the growing season in these crop regions.

5.2. NO_2 and PAN Fluxes. We estimate the fluxes of NO_2 and PAN at the canopy-level via eqs 10 and 11.

$$\text{Flux}_{\text{NO}_2} = 0.56G_c[\text{NO}_2] \quad (10)$$

$$\text{Flux}_{\text{PAN}} = 0.3G_c[\text{PAN}] \quad (11)$$

Figures 8 and 9 show estimates of the monthly integrated fluxes of NO_2 and PAN, respectively. Monthly fluxes were calculated by summing hourly fluxes during each day for a particular month. Hourly integrated fluxes were calculated by multiplying hourly NO_2 or PAN surface concentrations from WRF-Chem (see Section 2.4) with hourly calculated G_c . See supplement Figure S10 for midday fluxes calculated using

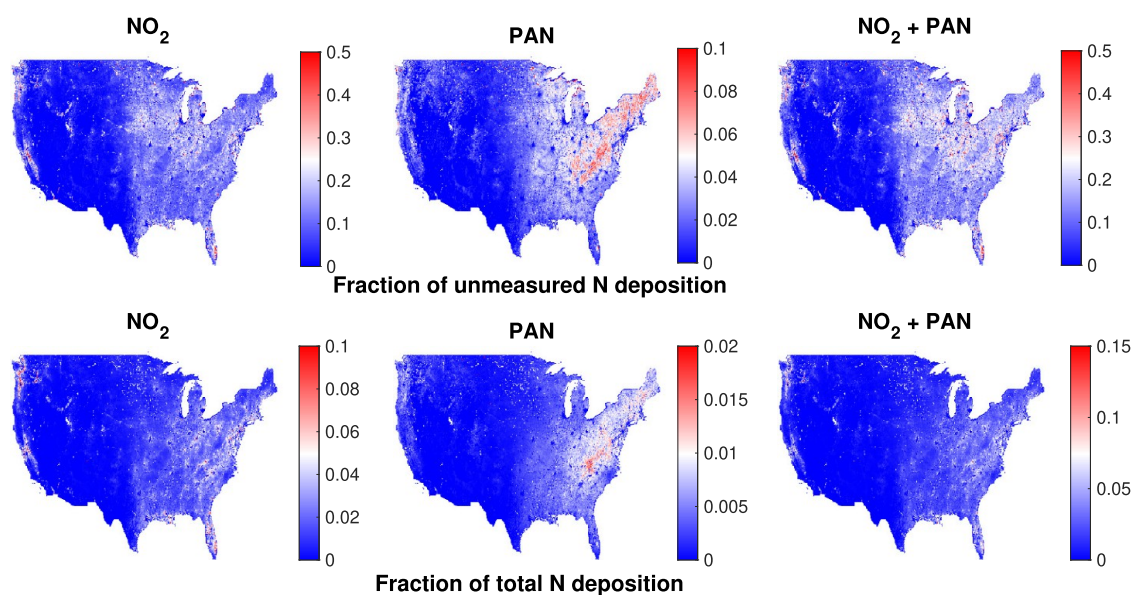


Figure 10. Yearly SIF-estimated stomatal (a) NO_2 fluxes, (b) PAN fluxes, and (c) $\text{NO}_2 + \text{PAN}$ fluxes as a fraction of the CASTNET CMAQ modeled estimates of total unmeasured nitrogen deposition over CONUS. Yearly SIF-estimated stomatal (d) NO_2 fluxes, (e) PAN fluxes, and (f) $\text{NO}_2 + \text{PAN}$ fluxes as a fraction of the CASTNET estimates of total nitrogen deposition over CONUS.

different methods for estimating surface NO_2 concentrations (GEOS-Chem, WRF-Chem, and TROPOMI NO_2). Hourly G_c was calculated by scaling the G_c at the time of TROPOMI's early afternoon overpass by the ratio of the light response parameter f_{light} at a particular time to f_{light} at the overpass time, where f_{light} is described by eq 12, derived from Emberson.¹²

$$f_{\text{light}} = 1 - \exp(\alpha \times \text{PPFD}_0 \times \cos(\text{SZA})) \quad (12)$$

PPFD_0 is the photosynthetic photon flux density (PPFD) at a solar zenith angle (SZA) of 0, approximately equal to $2200 \mu\text{mol m}^{-2} \text{s}^{-1}$.⁸⁷ The α parameter has been shown to vary from -0.01 to -0.003 depending on the plant species.⁸⁸ We set α equal to -0.005 to err on the side of underestimating G_c at lower daily light levels.

Our SIF- and WRF-derived fluxes of NO_2 show that the largest fluxes occur in agricultural and near-urban regions of the Midwest and Eastern Seaboard during the late summer, with maximum fluxes of over $0.1 \text{ kg N ha}^{-1} \text{ month}^{-1}$ (Figure 8). Substantial NO_2 fluxes ($0.1 \text{ kg N ha}^{-1} \text{ month}^{-1}$) can also be observed in the agricultural regions of California's Central Valley and the Pacific Northwest from April–August. Maximum yearly NO_2 fluxes reach up to $0.8 \text{ kg N ha}^{-1} \text{ year}^{-1}$ in the Central Valley and near-urban regions of the eastern United States. PAN fluxes are largest during the summer inland of East Coast cities, with maximum fluxes up to $0.02 \text{ kg N ha}^{-1} \text{ month}^{-1}$ and $0.1 \text{ kg N ha}^{-1} \text{ year}^{-1}$ (Figure 9). PAN deposition primarily occurs in the Eastern half of CONUS, driven by higher estimated concentrations of PAN in this region. These observations are consistent with field measurements and previous model simulations of PAN across CONUS.⁸⁹

In models, the limitation to the deposition rate introduced by turbulence and diffusion is represented as an aerodynamic resistance parameter. Aerodynamic resistances are typically 2–10 times less than the resistance associated with maximum stomatal diffusion of NO_2 and PAN during the daytime. Under the big-leaf model, which our approach resembles, aerodynamic resistances are typically less than 5 s cm^{-1} , with most

daytime values falling below 1 s cm^{-1} in a variety of regions.^{90–93} Aerodynamic resistances are largest in forests (regions of higher LAI) and under low wind speeds, particularly during the nighttime when we do not consider stomatal deposition.^{90–93} The error introduced by neglecting turbulence and diffusion is likely to be greater at larger G_c . We estimate that neglecting aerodynamic resistances could result in an over estimation of NO_2 and PAN annual fluxes by up to 30 and 10%, respectively (Figure S11). In addition to stomatal behavior, aerodynamic resistance is one of the most uncertain attributes of dry deposition estimates, with different parameterizations resulting in large differences in nitrogen dry deposition estimates, particularly for species such as HNO_3 that have a very low surface resistance to deposition.⁹²

The method we used to calculate monthly integrated G_c also assumes that the maximum canopy conductance occurs at the time of maximum light intensity. This assumption is likely to be accurate under most environmental conditions. However, in some semi-arid environments, such as many west coast forests, as soil and air moisture decline in the afternoon during the summer, stomata close in response, resulting in a daily maximum stomatal conductance occurring in the late morning, rather than early afternoon.¹⁶ Our method would result in an underestimation of deposition fluxes at locations with this behavior. Assuming maximum canopy conductance at the time of maximum PPFD would likely capture reductions in deposition due to heat stress, as the time of daily maximum temperature is likely to correspond to the time of maximum PPFD. An overestimation of fluxes could result, however, in cases where stomatal closure results from cold temperatures in the morning and evening, though this effect is likely to be minor during the growing season.

Nighttime stomatal deposition was not considered in the monthly and annual flux calculations, which may lead to underestimates of fluxes because the uptake of nitrogen oxides by stomata during the night has been identified as an important deposition process.⁷ The inclusion of winter months in the calculation of PAN and NO_2 annual fluxes also

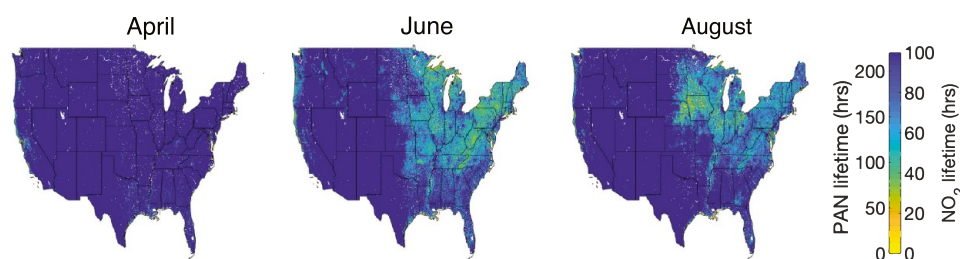


Figure 11. Average SIF-derived lifetimes of NO_2 and PAN to stomatal deposition over CONUS during (a) April, (b) June, and (c) August 2018 at the time of TROPOMI's overpass (13:30 LT).

introduces some uncertainty to the flux estimates, as discussed in Section 3.2. However, the much lower predicted canopy conductances during these months make the uncertainty in winter months unlikely to contribute substantially to the absolute uncertainty in yearly fluxes.

To date there are very few direct measurements of reactive nitrogen (N_r) dry deposition across CONUS.⁷⁸ As a result, regional estimates of N_r dry deposition are estimated either by coupling ambient measurements of N_r with inferential models or by running CTMs.^{83,94–96} Differences in model parameterizations of atmosphere–canopy exchange processes have been shown to result in substantially different fluxes of reactive nitrogen.^{78,92} Improved constraints on reactive nitrogen deposition fluxes are therefore needed. The National Atmospheric Deposition Program (NADP) through the Ammonia Monitoring Network (AMoN) and the Clean Air Status and Trends Network (CASTNET) monitor ambient concentrations and the wet deposition of nitrogen-containing compounds over CONUS and are frequently used for assessments of nitrogen deposition.⁹⁵ Measurements from these networks are coupled with the Community Multi-Scale Air Quality (CMAQ) model to estimate nitrogen wet and dry deposition as gaseous and particulate nitrate and ammonium, as well as the deposition of unmeasured gaseous species (e.g., NO_2 , PAN, HONO, and so forth).⁹⁵

In Figure 10, we compare our estimates of yearly PAN and NO_2 fluxes as a fraction of the unmeasured nitrogen deposition obtained from CASTNET CMAQ data and as a fraction of total nitrogen deposition. Our results indicate that deposition fluxes of NO_2 in particular may be up to 25–50% of unmeasured N_r deposition, as predicted by CMAQ in regions of the United States with substantial vegetation coverage (Figure 10). PAN is also found to constitute up to 10% of the total unmeasured nitrogen deposition in parts of the eastern United States. Near urban centers and in certain agricultural valleys, such as the Central Valley of California, NO_2 deposition can make up to 15% of the total nitrogen deposition as reported by CASTNET.

Our SIF-derived estimates of G_c , coupled with WRF estimates of NO_2 and PAN surface concentrations, represents a new method for constraining the fluxes of reactive nitrogen over large temporal and spatial scales. Such indirect measurements of G_c could potentially be combined with concentrations of NO_2 and PAN derived from other CTMs and observations (e.g., Figure S10). The analysis of residuals between the G_c -SIF model we present and other G_c models could also offer insights into the processes driving large-scale G_c , particularly as they relate to phenology. This method could also be easily extended to other depositing species shown to have deposition velocities that scale linearly with stomatal conductance.

5.3. NO_x and PAN Lifetime to Stomatal Deposition.

The lifetime of NO_x and PAN to stomatal uptake in the boundary layer can be estimated by dividing each species respective canopy conductance uptake rate by the planetary boundary layer (PBL) height. This approach for calculating a stomatal lifetime assumes that the stomatal uptake is rate-limiting and that the aerodynamic and boundary layer resistance are negligible compared to the stomatal deposition rate. Figure 11 shows the average lifetimes of NO_x and PAN to stomatal deposition at 13:30 local time for the months of April, June, and August 2018 across CONUS. Average monthly PBL heights for the months of April, June, and August across CONUS were calculated in WRF-Chem. Figure 11 indicates that NO_x lifetimes to stomatal uptake range from as low as 20 h to over 150 h across CONUS. The lifetime of PAN in the boundary layer is much longer (50–300 h) due to its lower stomatal uptake rate. The lifetimes of NO_x and PAN are typically shorter in areas of high biological activity (see Figure 5). However shorter lifetimes are also observed in coastal regions, such as the Pacific Northwest in the months of June and August, and this is due to the lower PBL heights in marine environments.

Satellite estimates of NO_x lifetime in major US cities have indicated that the lifetime of NO_x in urban environments ranges from ~ 1 to 8 h.^{97,98} This suggests that during the growing season, the deposition of NO_x to vegetation may compete with the chemical loss of NO_x to nitric acid or organic nitrates in certain regions. The lifetime of NO_x in rural regions has been difficult to probe directly but is estimated to be longer in these environments than urban environments. A study conducted by Romer et al. (2016) estimated that the photochemical lifetime of NO_x in an Alabama forest was 11 ± 5 h.⁹⁹ At this timescale and in a heavily forested environment, it is likely that deposition will be an important removal process of atmospheric NO_x . The stomatal removal of PAN from the atmosphere is less likely to be competitive with its thermochemical loss, which occurs on the timescale of < 10 h during warmer months. Deposition could however play an influential role in PAN removal when air temperatures are low ($T < 20$ °C). A complete assessment of the role of stomatal uptake in NO_x and PAN lifetimes is beyond the scope of this current work but could be an interesting extension to this work in a future investigation.

6. CONCLUSIONS

We developed a coupled SIF–GPP– G_c model to estimate G_c at 500 m spatial resolution across CONUS and demonstrate that SIF and GPP can also be used as a proxy for G_c . We then show how SIF-derived G_c can be used to estimate fluxes of NO_2 and PAN over CONUS.

In developing the SIF–GPP– G_c model, we show that GPP and G_c are correlated at a majority of sites across the Ameriflux network. This observed co-variation between GPP and G_c is consistent with the Ball–Berry framework. Correlations between GPP and G_c are highest at crop sites and lowest at wetland sites. We attribute the lower correlations at wetland sites to interference from surface evaporation in our estimation of G_c . Our analysis shows that on average, the GPP– G_c response can be described through a single slope of 0.036 [(cm s⁻¹ H₂O) (μmol⁻¹ CO₂ m² s)] for all ecosystem types.

By combining the empirical GPP– G_c relationship with the SIF–GPP model described by Turner et al. (2021), we were able to estimate G_c across CONUS using SIF retrievals from TROPOMI at the time of instrument overpass (13:30 LT). Key agricultural features such as the Central Valley in California and the Corn Belt in the Midwest are clearly discernible from space using the model. The monthly average G_c estimates we calculated were of comparable magnitude and spatial distribution to other midday estimates of G_c across CONUS during the growing season.

We combined our model with surface concentration estimates of NO₂ and PAN from WRF-Chem to estimate monthly and annual dry deposition fluxes of these species across CONUS for 2018. Using this method, we estimated maximum stomatal fluxes of 0.8 and 0.1 kg_N ha⁻¹ yr⁻¹ over CONUS for NO₂ and PAN, respectively. A comparison of our estimates of N_r dry deposition with CASTNET CMAQ suggests that the dry deposition of NO₂ and PAN may represent a substantial portion of unmeasured N_r deposition.

This work shows promise for constraining G_c with measurements of SIF in global atmospheric models. We propose that this model can serve as a useful tool for constraining regional canopy transpiration fluxes and the stomatal atmosphere–biosphere exchange of gases.

■ ASSOCIATED CONTENT

Supporting Information

The Supporting Information is available free of charge at <https://pubs.acs.org/doi/10.1021/acsearthspacechem.1c00260>.

Intercept and slope statistics for ecosystem-level and site-level relationships grouped by land classification; comparison of G_c values calculated with and without a stability correction; correlations between SIF– G_c , G_c –GPP, and SIF–GPP from 2018–2019; seasonal changes in leaf area index across CONUS as measured by MODIS; distribution of G_c /GPP ratios by ecosystem-type and all ecosystems; 2018 annual average G_c over CONUS at 13:30 LT; difference in NO₂ fluxes calculated with and without an intercept for January and June 2018; difference in yearly G_c and NO₂ fluxes calculated using ecosystem-specific slopes vs a single slope and an exponential model vs a linear model; comparison of NO₂ fluxes predicted by multiple combinations of models explored in this study; change in fluxes when aerodynamic resistance is assumed in the model; and statistics from the GPP– G_c fits performed using data collected from the Ameriflux sites used in this study (ZIP)

■ AUTHOR INFORMATION

Corresponding Author

Ronald C. Cohen – Department of Chemistry and Department of Earth and Planetary Science, University of California, Berkeley, Berkeley, California 94720, United States; orcid.org/0000-0001-6617-7691; Email: rccohen@berkeley.edu

Authors

Erin R. Delaria – Department of Chemistry, University of California, Berkeley, Berkeley, California 94720, United States; Atmospheric Chemistry and Dynamics Laboratory, NASA Goddard Space Flight Center, Greenbelt, Maryland 20771, United States; Earth System Science Interdisciplinary Center, University of Maryland, College Park, Maryland 20742, United States; orcid.org/0000-0002-6033-848X

Bryan K. Place – Department of Chemistry, University of California, Berkeley, Berkeley, California 94720, United States

Alexander J. Turner – Department of Earth and Planetary Science, University of California, Berkeley, Berkeley, California 94720, United States; Department of Atmospheric Sciences, University of Washington, Seattle, Washington 98195, United States; orcid.org/0000-0003-1406-7372

Qindan Zhu – Department of Earth and Planetary Science, University of California, Berkeley, Berkeley, California 94720, United States; orcid.org/0000-0003-2173-4014

Xiaomeng Jin – Department of Chemistry, University of California, Berkeley, Berkeley, California 94720, United States; orcid.org/0000-0002-6895-8464

Complete contact information is available at: <https://pubs.acs.org/doi/10.1021/acsearthspacechem.1c00260>

Author Contributions

#E.R.D. and B.K.P. equal first authors.

Notes

The authors declare no competing financial interest.

■ ACKNOWLEDGMENTS

This research was supported by the NOAA Climate Program Office's Atmospheric Chemistry, Carbon Cycle, and Climate Program (grant no. NA18OAR4310117) and the NASA Atmospheric Composition Modeling and Analysis Program (grant no. NNX15AE37G). A.J.T. was supported as a Miller Fellow with the Miller Institute for Basic Research in Science at UC Berkeley.

■ REFERENCES

- (1) IPCC. *Climate Change 2013: The Physical Science Basis. Contribution of Working Group I to the Fifth Assessment Report of the Intergovernmental Panel on Climate Change*; Technical Report, 2013.
- (2) Schlesinger, W. H.; Jasechko, S. Transpiration in the global water cycle. *Agric. For. Meteorol.* **2014**, *189–190*, 115–117.
- (3) Cowan, I. R. In *Stomatal Behaviour and Environment. Advances in Botanical Research*; Preston, R., Woolhouse, H., Eds.; Academic Press, 1978; Vol. 4, pp 117–228.
- (4) Green, S. Radiation balance, transpiration and photosynthesis of an isolated tree. *Agric. For. Meteorol.* **1993**, *64*, 201–221.
- (5) Tuzet, A.; Perrier, A.; Leuning, R. A coupled model of stomatal conductance, photosynthesis and transpiration. *Plant, Cell Environ.* **2003**, *26*, 1097–1116.
- (6) Miner, G. L.; Bauerle, W. L. Seasonal variability of the parameters of the Ball–Berry model of stomatal conductance in maize (*Zea mays* L.) and sunflower (*Helianthus annuus* L.) under well-

watered and water-stressed conditions. *Plant, Cell Environ.* **2017**, *40*, 1874–1886.

(7) Delaria, E. R.; Place, B. K.; Liu, A. X.; Cohen, R. C. Laboratory measurements of stomatal NO₂ deposition to native California trees and the role of forests in the NO_x cycle. *Atmos. Chem. Phys. Discuss.* **2020**, *20*, 14023–14041.

(8) Place, B. K.; Delaria, E. R.; Liu, A. X.; Cohen, R. C. Leaf Stomatal Control over Acyl Peroxynitrate Dry Deposition to Trees. *ACS Earth Space Chem.* **2020**, *4*, 2162–2170.

(9) Guenther, A.; Jiang, X.; Heald, C.; Sakulyanontvittaya, T.; Duhl, T.; Emmons, L.; Wang, X. The Model of Emissions of Gases and Aerosols from Nature version 2.1 (MEGAN2.1): an extended and updated framework for modeling biogenic emissions. *Geosci. Model Dev. Discuss.* **2012**, *5*, 1471.

(10) Saunio, M.; et al. The Global Methane Budget: 2000–2012. *Earth Syst. Sci. Data Discuss.* **2016**, *8*, 697–751.

(11) Huang, G.; Brook, R.; Crippa, M.; Janssens-Maenhout, G.; Schieberle, C.; Dore, C.; Guizzardi, D.; Muntean, M.; Schaaf, E.; Friedrich, R. Speciation of anthropogenic emissions of non-methane volatile organic compounds: a global gridded data set for 1970–2012. *Atmos. Chem. Phys.* **2017**, *17*, 7683–7701.

(12) Emberson, L. D.; Wieser, G.; Ashmore, M. R. Modelling of stomatal conductance and ozone flux of Norway spruce: comparison with field data. *Environ. Pollut.* **2000**, *109*, 393–402.

(13) Clifton, O. E.; et al. Dry Deposition of Ozone Over Land: Processes, Measurement, and Modeling. *Rev. Geophys.* **2020**, *58*, No. e2019RG000670.

(14) Yienger, J. J.; Levy, H. Empirical model of global soil-biogenic NO_x emissions. *J. Geophys. Res.: Atmos.* **1995**, *100*, 11447–11464.

(15) Lerday, M. T.; Munger, J. W.; Jacob, D. J. The NO₂ Flux Conundrum. *Science* **2000**, *289*, 2291–2293.

(16) Delaria, E. R.; Cohen, R. C. A model-based analysis of foliar NO_x deposition. *Atmos. Chem. Phys.* **2020**, *20*, 2123–2141.

(17) Kavassalis, S.; Murphy, J. Understanding ozone-meteorology correlations: A role for dry deposition. *Geophys. Res. Lett.* **2017**, *44*, 2922.

(18) Gunderson, C. A.; Sholtis, J. D.; Wullschlegel, S. D.; Tissue, D. T.; Hanson, P. J.; Norby, R. J. Environmental and stomatal control of photosynthetic enhancement in the canopy of a sweetgum (*Liquidambar styraciflua* L.) plantation during 3 years of CO₂ enrichment. *Plant, Cell Environ.* **2002**, *25*, 379–393.

(19) Altimir, N.; Tuovinen, J.-P.; Vesala, T.; Kulmala, M.; Hari, P. Measurements of ozone removal by Scots pine shoots: Calibration of a stomatal uptake model including the non-stomatal component. *Atmos. Environ.* **2004**, *38*, 2387–2398.

(20) Hardacre, C.; Wild, O.; Emberson, L. An evaluation of ozone dry deposition in global scale chemistry climate models. *Atmos. Chem. Phys.* **2015**, *15*, 6419–6436.

(21) Medlyn, B. E.; Duursma, R. A.; Eamus, D.; Ellsworth, D. S.; Prentice, I. C.; Barton, C. V. M.; Crous, K. Y.; De Angelis, P.; Freeman, M.; Wingate, L. Reconciling the optimal and empirical approaches to modelling stomatal conductance. *Global Change Biol.* **2011**, *17*, 2134–2144.

(22) Bonan, G. B.; Williams, M.; Fisher, R. A.; Oleson, K. W. Modeling stomatal conductance in the Earth system: Linking leaf water-use efficiency and water transport along the soil-plant-atmosphere continuum. *Geosci. Model Dev.* **2014**, *7*, 2193–2222.

(23) Cleugh, H. A.; Leuning, R.; Mu, Q.; Running, S. W. Regional evaporation estimates from flux tower and MODIS satellite data. *Remote Sens. Environ.* **2007**, *106*, 285–304.

(24) Kalma, J. D.; McVicar, T. R.; McCabe, M. F. Estimating land surface evaporation: a review of methods using remotely sensed surface temperature data. *Surv. Geophys.* **2008**, *29*, 421–469.

(25) Moran, M. S.; Jackson, R. D. Assessing the spatial distribution of evapotranspiration using remotely sensed inputs. *J. Environ. Qual.* **1991**, *20*, 725–737.

(26) Shan, N.; Ju, W.; Migliavacca, M.; Martini, D.; Guanter, L.; Chen, J.; Goulas, Y.; Zhang, Y. Modeling canopy conductance and

transpiration from solar-induced chlorophyll fluorescence. *Agric. For. Meteorol.* **2019**, *268*, 189–201.

(27) Glenn, E. P.; Nagler, P. L.; Huete, A. R. Vegetation index methods for estimating evapotranspiration by remote sensing. *Surv. Geophys.* **2010**, *31*, 531–555.

(28) Glenn, E. P.; Doody, T. M.; Guerschman, J. P.; Huete, A. R.; King, E. A.; McVicar, T. R.; Van Dijk, A. I. J. M.; Van Niel, T. G.; Yebra, M.; Zhang, Y. Actual evapotranspiration estimation by ground and remote sensing methods: the Australian experience. *Hydrol. Process.* **2011**, *25*, 4103–4116.

(29) Glenn, E. P.; Neale, C. M. U.; Hunsaker, D. J.; Nagler, P. L. Vegetation index-based crop coefficients to estimate evapotranspiration by remote sensing in agricultural and natural ecosystems. *Hydrol. Process.* **2011**, *25*, 4050–4062.

(30) Yebra, M.; Van Dijk, A.; Leuning, R.; Huete, A.; Guerschman, J. P. Evaluation of optical remote sensing to estimate actual evapotranspiration and canopy conductance. *Remote Sens. Environ.* **2012**, *129*, 250–261.

(31) Barraza, V.; Restrepo-Coupe, N.; Huete, A.; Grings, F.; Van Gorsel, E. Passive microwave and optical index approaches for estimating surface conductance and evapotranspiration in forest ecosystems. *Agric. For. Meteorol.* **2015**, *213*, 126–137.

(32) Shan, N.; Zhang, Y.; Chen, J. M.; Ju, W.; Migliavacca, M.; Peñuelas, J.; Yang, X.; Zhang, Z.; Nelson, J. A.; Goulas, Y. A model for estimating transpiration from remotely sensed solar-induced chlorophyll fluorescence. *Remote Sens. Environ.* **2021**, *252*, 112134.

(33) Maes, W. H.; Pagán, B. R.; Martens, B.; Gentile, P.; Guanter, L.; Steppe, K.; Verhoest, N. E. C.; Dorigo, W.; Li, X.; Xiao, J.; Miralles, D. G. Sun-induced fluorescence closely linked to ecosystem transpiration as evidenced by satellite data and radiative transfer models. *Remote Sens. Environ.* **2020**, *249*, 112030.

(34) Monteith, J. Evaporation and Environment. *Symposia of the Society for Experimental Biology*, 1965; Vol. 19, pp 205–234.

(35) Monteith, J. L. *Principles of Environmental Physics*; Edward Arnold Limited, 1973.

(36) Hatfield, J.; Perrier, A.; Jackson, R. Estimation of evapotranspiration at one time-of-day using remotely sensed surface temperatures. *Agricultural Water Management* **1983**, *7*, 341–350.

(37) Leuning, R.; van Gorsel, E.; Massman, W. J.; Isaac, P. R. Reflections on the surface energy imbalance problem. *Agric. For. Meteorol.* **2012**, *156*, 65–74.

(38) Wehr, R.; Saleska, S. R. Calculating canopy stomatal conductance from eddy covariance measurements, in light of the energy budget closure problem. *Biogeosciences* **2021**, *18*, 13–24.

(39) Hu, X.; Shi, L.; Lin, G. The data-driven solution of energy imbalance-induced structural error in evapotranspiration models. *J. Hydrol.* **2021**, *597*, 126205.

(40) Damm, A.; Haghghi, E.; Paul-Limoges, E.; van der Tol, C. On the seasonal relation of sun-induced chlorophyll fluorescence and transpiration in a temperate mixed forest. *Agric. For. Meteorol.* **2021**, *304–305*, 108386.

(41) Reichstein, M.; et al. On the separation of net ecosystem exchange into assimilation and ecosystem respiration: review and improved algorithm. *Global Change Biol.* **2005**, *11*, 1424–1439.

(42) Veeckind, J. P.; et al. TROPOMI on the ESA Sentinel-5 Precursor: A GMES mission for global observations of the atmospheric composition for climate, air quality and ozone layer applications. *Remote Sens. Environ.* **2012**, *120*, 70–83 The Sentinel Missions—New Opportunities for Science.

(43) Köhler, P.; Frankenberg, C.; Magney, T. S.; Guanter, L.; Joiner, J.; Landgraf, J. Global Retrievals of Solar-Induced Chlorophyll Fluorescence With TROPOMI: First Results and Intersensor Comparison to OCO-2. *Geophys. Res. Lett.* **2018**, *45*, 10456–10463.

(44) Turner, A. J.; Köhler, P.; Magney, T. S.; Frankenberg, C.; Fung, I.; Cohen, R. C. A double peak in the seasonality of California's photosynthesis as observed from space. *Biogeosciences* **2020**, *17*, 405–422.

(45) Turner, A. J.; Köhler, P.; Magney, T. S.; Frankenberg, C.; Fung, I.; Cohen, R. C. Extreme events driving year-to-year differences in

gross primary productivity across the US. *Biogeosci. Discuss.* **2021**, *2021*, 1–13.

(46) Zare, A.; Romer, P. S.; Nguyen, T.; Keutsch, F. N.; Skog, K.; Cohen, R. C. A comprehensive organic nitrate chemistry: insights into the lifetime of atmospheric organic nitrates. *Atmos. Chem. Phys.* **2018**, *18*, 15419–15436.

(47) Buchholz, R. R.; Emmons, L. K.; Tilmes, S.; Team, T. C. D. *CESM2.1/CAM-chem Instantaneous Output for Boundary Conditions*; UCAR/NCAR—Atmospheric Chemistry Observations and Modeling Laboratory, 2021.

(48) Emmons, L. K.; et al. The Chemistry Mechanism in the Community Earth System Model Version 2 (CESM2). *J. Adv. Model. Earth Syst.* **2020**, *12*, No. e2019MS001882.

(49) EPA. Air Pollutant Emissions Trends Data. 2016, <https://www.epa.gov/air-emissions-inventories/air-pollutant-emissions-trends-data>.

(50) Travis, K. R.; et al. Why do models overestimate surface ozone in the Southeast United States? *Atmos. Chem. Phys.* **2016**, *16*, 13561–13577.

(51) Fisher, J. A.; et al. Organic nitrate chemistry and its implications for nitrogen budgets in an isoprene- and monoterpene-rich atmosphere: constraints from aircraft (SEAC⁴RS) and ground-based (SOAS) observations in the Southeast US. *Atmos. Chem. Phys.* **2016**, *16*, 5969–5991.

(52) Magney, T. S.; Bowling, D. R.; Logan, B. A.; Grossmann, K.; Stutz, J.; Blanken, P. D.; Burns, S. P.; Cheng, R.; Garcia, M. A.; Köhler, P.; Lopez, S.; Parazoo, N. C.; Raczka, B.; Schimel, D.; Frankenberg, C. Mechanistic evidence for tracking the seasonality of photosynthesis with solar-induced fluorescence. *Proc. Natl. Acad. Sci. U.S.A.* **2019**, *116*, 11640–11645.

(53) He, L.; Magney, T.; Dutta, D.; Yin, Y.; Köhler, P.; Grossmann, K.; Stutz, J.; Dold, C.; Hatfield, J.; Guan, K.; Peng, B.; Frankenberg, C. From the Ground to Space: Using Solar-Induced Chlorophyll Fluorescence to Estimate Crop Productivity. *Geophys. Res. Lett.* **2020**, *47*, No. e2020GL087474.

(54) Marrs, J. K.; Reblin, J. S.; Logan, B. A.; Allen, D. W.; Reinmann, A. B.; Bombard, D. M.; Tabachnik, D.; Hutyrta, L. R. Solar-Induced Fluorescence Does Not Track Photosynthetic Carbon Assimilation Following Induced Stomatal Closure. *Geophys. Res. Lett.* **2020**, *47*, No. e2020GL087956.

(55) Maguire, A. J.; Eitel, J. U. H.; Griffin, K. L.; Magney, T. S.; Long, R. A.; Vierling, L. A.; Schmiede, S. C.; Jennewein, J. S.; Weygint, W. A.; Boelman, N. T.; Bruner, S. G. On the Functional Relationship Between Fluorescence and Photochemical Yields in Complex Evergreen Needleleaf Canopies. *Geophys. Res. Lett.* **2020**, *47*, No. e2020GL087858.

(56) Magney, T. S.; Barnes, M. L.; Yang, X. On the Covariation of Chlorophyll Fluorescence and Photosynthesis Across Scales. *Geophys. Res. Lett.* **2020**, *47*, No. e2020GL091098.

(57) Ball, J. T.; Woodrow, I. E. In *Progress in Photosynthesis Research 7th International Congress*; Biggins, J., Ed.; Martinus Nijhoff Publishers: Dordrecht, Netherlands, 1988.

(58) Leuning, R. Modelling stomatal behaviour and photosynthesis of *Eucalyptus grandis*. *Funct. Plant Biol.* **1990**, *17*, 159–175.

(59) Collatz, G.; Ribas-Carbo, M.; Berry, J. Coupled photosynthesis-stomatal conductance model for leaves of C₄ plants. *Funct. Plant Biol.* **1992**, *19*, 519–538.

(60) Leuning, R. A critical appraisal of a combined stomatal-photosynthesis model for C₃ plants. *Plant, Cell Environ.* **1995**, *18*, 339–355.

(61) Lai, C.-T.; Katul, G.; Oren, R.; Ellsworth, D.; Schäfer, K. Modeling CO₂ and water vapor turbulent flux distributions within a forest canopy. *J. Geophys. Res.* **2000**, *105*, 26333–26351.

(62) Valentini, R.; Gamon, J. A.; Field, C. B. Ecosystem gas exchange in a California grassland: seasonal patterns and implications for scaling. *Ecology* **1995**, *76*, 1940–1952.

(63) Wolf, A.; Akshalov, K.; Saliendra, N.; Johnson, D. A.; Laca, E. A. Inverse estimation of V_{c,max}, leaf area index and the Ball-Berry parameter from carbon and energy fluxes. *J. Geophys. Res.* **2006**, *111*, D08S08.

(64) Launiainen, S.; Katul, G. G.; Kolari, P.; Vesala, T.; Hari, P. Empirical and optimal stomatal controls on leaf and ecosystem level CO₂ and H₂O exchange rates. *Agric. For. Meteorol.* **2011**, *151*, 1672–1689.

(65) Ono, K.; Maruyama, A.; Kuwagata, T.; Mano, M.; Takimoto, T.; Hayashi, K.; Hasegawa, T.; Miyata, A. Canopy-scale relationships between stomatal conductance and photosynthesis in irrigated rice. *Global Change Biol.* **2013**, *19*, 2209–2220.

(66) Sellers, P. J.; Heiser, M. D.; Hall, F. G. Relations between surface conductance and spectral vegetation indices and intermediate (100 m² to 15 km²) length scales. *J. Geophys. Res.* **1992**, *97*, 19033–19059.

(67) Miner, G. L.; Bauerle, W. L.; Baldocchi, D. D. Estimating the sensitivity of stomatal conductance to photosynthesis. *Plant, Cell Environ.* **2017**, *40*, 1214–1238.

(68) Barnard, D. M.; Bauerle, W. L. The implications of minimum stomatal conductance on modeling water flux in forest canopies. *J. Geophys. Res.: Biogeosci.* **2013**, *118*, 1322–1333.

(69) Baker, I.; Denning, S.; Stöckli, R. North American gross primary productivity: regional characterization and interannual variability. *Tellus B* **2010**, *62*, 533–549.

(70) Wesely, M. L. Parameterization of surface resistances to gaseous dry deposition in regional-scale numerical models. *Atmos. Environ.* **1989**, *23*, 1293–1304.

(71) Knauer, J.; Werner, C.; Zaehle, S. Evaluating stomatal models and their atmospheric drought response in a land surface scheme: A multi-biome analysis. *J. Geophys. Res.: Biogeosci.* **2015**, *120*, 1894–1911.

(72) Kennedy, D.; Swenson, S.; Oleson, K.; Fisher, R.; Lawrence, D.; da Costa, A.; Gentile, P. Implementing Plant Hydraulics in the Community Land Model, Version 5. *J. Adv. Model. Earth Syst.* **2019**, *11*, 485.

(73) Mekonnen, Z. A.; Grant, R. F.; Schwalm, C. Contrasting changes in gross primary productivity of different regions of North America as affected by warming in recent decades. *Agric. For. Meteorol.* **2016**, *218–219*, 50–64.

(74) Jiang, Y.; Still, C. J.; Rastogi, B.; Page, G. F. M.; Wharton, S.; Meinzer, F. C.; Voelker, S.; Kim, J. B. Trends and controls on water-use efficiency of an old-growth coniferous forest in the Pacific Northwest. *Environ. Res. Lett.* **2019**, *14*, 074029.

(75) Jonard, F.; De Cannière, S.; Brüggemann, N.; Gentile, P.; Short Gianotti, D. J.; Lobet, G.; Miralles, D. G.; Montzka, C.; Pagán, B. R.; Rascher, U.; Vereecken, H. Value of sun-induced chlorophyll fluorescence for quantifying hydrological states and fluxes: Current status and challenges. *Agric. For. Meteorol.* **2020**, *291*, 108088.

(76) Canadian Air and Precipitation Monitoring Network. <http://data.ec.gc.ca/data/air/monitor/networks-and-studies/canadian-air-and-precipitation-monitoring-network-capmon/> (accessed 5 May 2021).

(77) National Atmospheric Deposition Program. <http://nadp.slh.wisc.edu/> (accessed 20 April 2021).

(78) Walker, J. T.; Beachley, G.; Zhang, L.; Benedict, K. B.; Sive, B. C.; Schwede, D. B. A review of measurements of air-surface exchange of reactive nitrogen in natural ecosystems across North America. *Sci. Total Environ.* **2019**, *698*, 133975.

(79) Vet, R.; et al. A global assessment of precipitation chemistry and deposition of sulfur, nitrogen, sea salt, base cations, organic acids, acidity and pH, and phosphorus. *Atmos. Environ.* **2013**, *93*, 3–100.

(80) Zhang, L.; Jacob, D. J.; Knipping, E. M.; Kumar, N.; Munger, J. W.; Carouge, C. C.; van Donkelaar, A.; Wang, Y. X.; Chen, D. Nitrogen deposition to the United States: distribution, sources, and processes. *Atmos. Chem. Phys.* **2012**, *12*, 4539–4554.

(81) Zhang, Y.; Mathur, R.; Bash, J. O.; Hogrefe, C.; Xing, J.; Roselle, S. J. Long-term trends in total inorganic nitrogen and sulfur deposition in the US from 1990 to 2010. *Atmos. Chem. Phys.* **2018**, *18*, 9091–9106.

(82) Du, E.; de Vries, W.; Galloway, J. N.; Hu, X.; Fang, J. Changes in wet nitrogen deposition in the United States between 1985 and 2012. *Environ. Res. Lett.* **2014**, *9*, 095004.

(83) Li, Y.; Schichtel, B. A.; Walker, J. T.; Schwede, D. B.; Chen, X.; Lehmann, C. M. B.; Puchalski, M. A.; Gay, D. A.; Collett, J. L. Increasing importance of deposition of reduced nitrogen in the United States. *Proc. Natl. Acad. Sci. U.S.A.* **2016**, *113*, 5874–5879.

(84) Sparks, J. P.; Roberts, J. M.; Monson, R. K. The uptake of gaseous organic nitrogen by leaves: A significant global nitrogen transfer process. *Geophys. Res. Lett.* **2003**, *30*, 2189.

(85) Teklemariam, T. A.; Sparks, J. P. Gaseous fluxes of peroxyacetyl nitrate (PAN) into plant leaves. *Plant, Cell Environ.* **2004**, *27*, 1149–1158.

(86) Chaparro-Suarez, I. G.; Meixner, F. X.; Kesselmeier, J. Nitrogen dioxide (NO₂) uptake by vegetation controlled by atmospheric concentrations and plant stomatal aperture. *Atmos. Environ.* **2011**, *45*, 5742–5750.

(87) Madronich, S.; Flocke, S. In *Environmental Photochemistry*; Boule, P., Ed.; Springer Berlin Heidelberg: Berlin, Heidelberg, 1999; pp 1–26.

(88) Büker, P.; et al. DO₃SE modelling of soil moisture to determine ozone flux to forest trees. *Atmos. Chem. Phys.* **2012**, *12*, 5537–5562.

(89) Fischer, E. V.; Jacob, D. J.; Yantosca, R. M.; Sulprizio, M. P.; Millet, D. B.; Mao, J.; Paulot, F.; Singh, H. B.; Roiger, A.; Ries, L.; Talbot, R. W.; Dzepina, K.; Pandey Deolal, S. Atmospheric peroxyacetyl nitrate (PAN): a global budget and source attribution. *Atmos. Chem. Phys.* **2014**, *14*, 2679–2698.

(90) Padro, J. Summary of ozone dry deposition velocity measurements and model estimates over vineyard, cotton, grass and deciduous forest in summer. *Atmos. Environ.* **1996**, *30*, 2363–2369.

(91) Zhang, L.; Brook, J. R.; Vet, R. A revised parameterization for gaseous dry deposition in air-quality models. *Atmos. Chem. Phys.* **2003**, *3*, 2067–2082.

(92) Schwede, D.; Zhang, L.; Vet, R.; Lear, G. An intercomparison of the deposition models used in the CASTNET and CAPMoN networks. *Atmos. Environ.* **2011**, *45*, 1337–1346.

(93) Liu, S.; Mao, D.; Lu, L. Measurement and estimation of the aerodynamic resistance. *Hydrol. Earth Syst. Sci. Discuss.* **2006**, *3*, 681–705.

(94) Sickles, J. E., II; Shadwick, D. S. Air quality and atmospheric deposition in the eastern US: 20 years of change. *Atmos. Chem. Phys.* **2015**, *15*, 173–197.

(95) Schwede, D. B.; Lear, G. G. A novel hybrid approach for estimating total deposition in the United States. *Atmos. Environ.* **2014**, *92*, 207–220.

(96) Bowker, G.; Schwede, D.; Lear, G.; Warren-Hicks, W.; Finkelstein, P. Quality Assurance Decisions with Air Models: A Case Study of Imputation of Missing Input Data Using EPA's Multi-layer Model. *Water, Air, Soil Pollut.* **2011**, *222*, 391.

(97) Laughner, J. L.; Cohen, R. C. Direct observation of changing NO_x lifetime in North American cities. *Science* **2019**, *366*, 723–727.

(98) Liu, F.; Beirle, S.; Zhang, Q.; Dörner, S.; He, K.; Wagner, T. NO_x lifetimes and emissions of cities and power plants in polluted background estimated by satellite observations. *Atmos. Chem. Phys.* **2016**, *16*, 5283–5298.

(99) Romer, P. S.; et al. The lifetime of nitrogen oxides in an isoprene-dominated forest. *Atmos. Chem. Phys.* **2016**, *16*, 7623–7637.